SUPPORTING INFORMATION

Strongly Confined Excitons in GaN/AlN Nanostructures with Atomically Thin GaN Layers for Efficient Light Emission in Deep-Ultraviolet

A.A. Toropov*[†], E. A. Evropeitsev[†], M. O. Nestoklon[†], D. S. Smirnov[†], T. V. Shubina[†], V. Kh. Kaibyshev[†], G. V. Budkin[†], V. N. Jmerik[†], D. V. Nechaev[†], S. Rouvimov[‡], S. V. Ivanov[†], and B. Gil[†,§]

[†] Ioffe Institute, St. Petersburg 194021, Russia

[‡]University of Notre Dame, Notre Dame, Indiana 46556, USA

[§]Université Montpellier, L2C, UMR 5221, 34095 Cedex 5 Montpellier, France

*E-mail: toropov@beam.ioffe.ru

1 Overview of room temperature exciton radiative lifetime in 2D systems

The effective exciton radiative decay rate at elevated temperatures is given by an average over the thermal distribution, resulting in the lifetime which increases linearly with temperature. At a given temperature, the effective radiative decay time in a two-dimensional (2D) structure like a quantum well (QW) reads [1,2,3]

$$\tau_{rad}^{eff} = \frac{3}{2}\frac{k_B T}{E_0}\tau_{rad}^{0}, \quad (1)$$

where $\tau_{rad}^{0} = \frac{1}{2\Gamma_0}$ is the radiative lifetime at the in-plane exciton wave-vector $\boldsymbol{k}_{\parallel} = 0$, Γ_0 is the respective decay rate, $E_0 = \frac{(\hbar k_0)^2}{2M}$ represents the "radiative window" where the excitons can decay radiatively without changing their in-plane wave-vector, $k_0 = \frac{E_{ex}\sqrt{\varepsilon}}{\hbar c}$ is the light wave-vector in the sample (ε is the dielectric constant, E_{ex} is the exciton transition energy, c - the speed of light in vacuum), $M = m_e + m_h$ is the exciton mass. In the approximation of high barriers and moderately thin QWs, the intrinsic exciton radiative lifetime τ_{rad}^{0} can be estimated as [4]

$$\tau_{rad}^{0}{}^{-1} = 8 a_B k_0 \omega_{LT}, \quad (2)$$

where a_B and ω_{LT} are the 3D exciton Bohr radius and longitudinal-transverse splitting in the bulk material, respectively.

The quasi-2D exciton confinement was first implemented in III-V semiconductor QW heterostructures [5]. For the excitons confined in a most common GaAs/AlGaAs QW, the intrinsic radiative lifetime τ_{rad}^0 measured at low temperatures can be as short as ~10-20 ps [6,7]. However, width of the radiative window estimated for the parameters of GaAs [8] is as small as ~70 μeV and the effective radiative lifetime estimated from Eq. (1) for 300 K is as long as 11-14 ns. In fact, this theoretical limit of the lifetimes of free excitons has never been observed in III-V QWs due to the nonradiative recombination, whose rate is drastically enhanced at elevated temperatures, resulting in a drop of the emission yield [9].

In the last years, the extreme 2D confinement of the carriers and excitons was realized in monolayers (MLs) of transition metal dichalcogenides (TMDs) of the generalized formula MX_2 (M = Mo, W; X = S, Se, Te). Single MLs of MX_2 materials are very much appropriate for that as they are mostly the direct-gap semiconductors in contrast to their bulk counterparts that are materials with the indirect band gaps [10]. Thanks to this ultimate thinness, large effective masses of carriers and reduced electrical screening, the exciton binding energy for such MLs can be as large as several hundreds of meV that gives rise to existence of the tightly bound 2D excitons up to room temperature [11,12]. The intrinsic radiative lifetime τ_{rad}^0 measured at low temperatures in a ML of $MoSe_2$, which is a representative of 2D TMDs, is an order of magnitude shorter than in III-V QWs, being less than 2 ps [13]. However, the width of the radiative window in this material is also much smaller, being about 13 μeV, that is due to the smaller dielectric constant and larger effective masses at a comparable exciton transition energy [13,14]. As a result, the effective radiative lifetime estimated for 300 K is of the order of 6 ns. The lifetime of the excitonic photoluminescence (PL), measured at 300 K in the ML of $MoSe_2$, was shorter than 1 ns, clearly indicating dominant contribution of nonradiative channels and greatly reduced emission yield. Thus, to the best of our knowledge, neither of the state-of-the-art 2D semiconductor materials is optimal for the room-temperature application as an efficient light-emitter based on strongly confined 2D excitons.

At present, there are no available data on the exciton lifetime in 2D GaN/AlN heterostructures. Nevertheless, one can assume that the wide-bandgap semiconductors GaN and AlN should be especially appropriate for designing efficient room-temperature excitonic emitters, since the width of the radiative window E_0 is proportional to the squared exciton transition energy E_{ex}. To illustrate the potential advantages of the 2D GaN/AlN structure, we represent schematically in Figure 1 of the main text the lowest-energy bright exciton dispersion curve in the exciton zone center for both a ML of $MoSe_2$, and a hypothetical 2D structure with all relevant

parameters of GaN [15] and the exciton transition energy equal to 5.4 eV as in Refs. [16,17]. It is clear from the plots that for the GaN-based structure the width of the radiative window ($E_0 \sim 290$) μeV is ~22 times larger than for the $MoSe_2$ ML, owing to the 3.2 times larger exciton transition energy. Substituting in Eq. (1) this value of E_0 and the intrinsic lifetime τ_{rad}^0 estimated with Eq. (2) as 0.6 ps, we obtain the effective radiative lifetime for 300°K as short as 130 ps.

2 Fabrication and PL spectroscopy of ultra-narrow GaN/AlN QWs

Plasma-assisted molecular beam epitaxy (MBE) was used to fabricate single insertions of GaN in AlN with intended thicknesses of 1-4 MLs. The structures were grown with a Compact 21T (Riber) MBE setup on standard annealed and nitridated c-sapphire substrates [17]. To reduce density of threading dislocations, an AlN buffer layer with a thickness of ~1.5 μm was first grown at a substrate temperature T_S =780°C under Al-rich conditions [18]. Then, the GaN/AlN QW structure was grown at T_S =700°C under metal-rich conditions at flux ratios of F_{Ga}/F_N~2 and F_{Al}/F_N~1.05. Finally, a 35 nm thick AlN cap layer was deposited at T_S=770-780°C. During growth, the layers thicknesses and surface morphology were monitored in situ by reflection high-energy electron diffraction, optical laser reflection, and a home-made multi-beam optical stress sensor. To make sure that all samples have identical properties except the thickness of the GaN insertion, the optical experiments were performed on the samples, where rotation of the substrate was switched off during the QW growth, which resulted in a gradient of the QW thickness along a certain direction over the sample surface. Most of the experimental data presented in the paper were obtained using one stripe of a sample, cut parallel to the grade direction. The PL spectra and decays were measured at the different spot positions along this stripe.

After growth, an atomic level structure analysis was performed with FEI Titan 80-300 transmission electron microscope (TEM) with a resolution of 0.136 nm in scanning TEM (STEM) mode and about 0.1 nm information limit in high resolution TEM mode. The cross-sectional TEM specimens were prepared using a Helios Nano Lab 600 system equipped with a FIB setup. For all gradient samples we investigated, the high angle annular dark field (HAADF) STEM studies were performed on a second (reference) stripe cut adjacent to the preceding one used in the PL experiments that permitted us to calibrate the average GaN thickness for each sample in a few selected points along the thickness gradient.

For the PL measurements, we used as an excitation source the fourth harmonics of a mode-locked Ti:Sapphire laser (COHERENT MIRA900 with HARMONICS BOX GENERATOR), providing pulsed excitation of 120 fs duration with a wavelength of typically 210 nm at a repetition frequency of 75 MHz. This excitation wavelength corresponds to a below-barrier, quasi-resonant

excitation of the QW emission. The sample was mounted within a He-flow optical micro-cryostat Janis ST-500, allowing temperature control in the range of 5 – 300 K. The excitation spot size was about 10 μm and the average excitation power density did not exceed 2 W/cm^2. The spectra were detected with a grating spectrometer (Princeton Instruments, Acton SP2500, 1800 lines/mm) equipped with a cooled CCD camera. The measured PL spectra were corrected for the system-response function. The PL decay was detected with a fast photomultiplier module (Becker&Hickl, PMC-150) coupled to a time-correlated single photon counting system (Becker&Hickl, SPC130). Direct time resolution of the setup was ~140 ps.

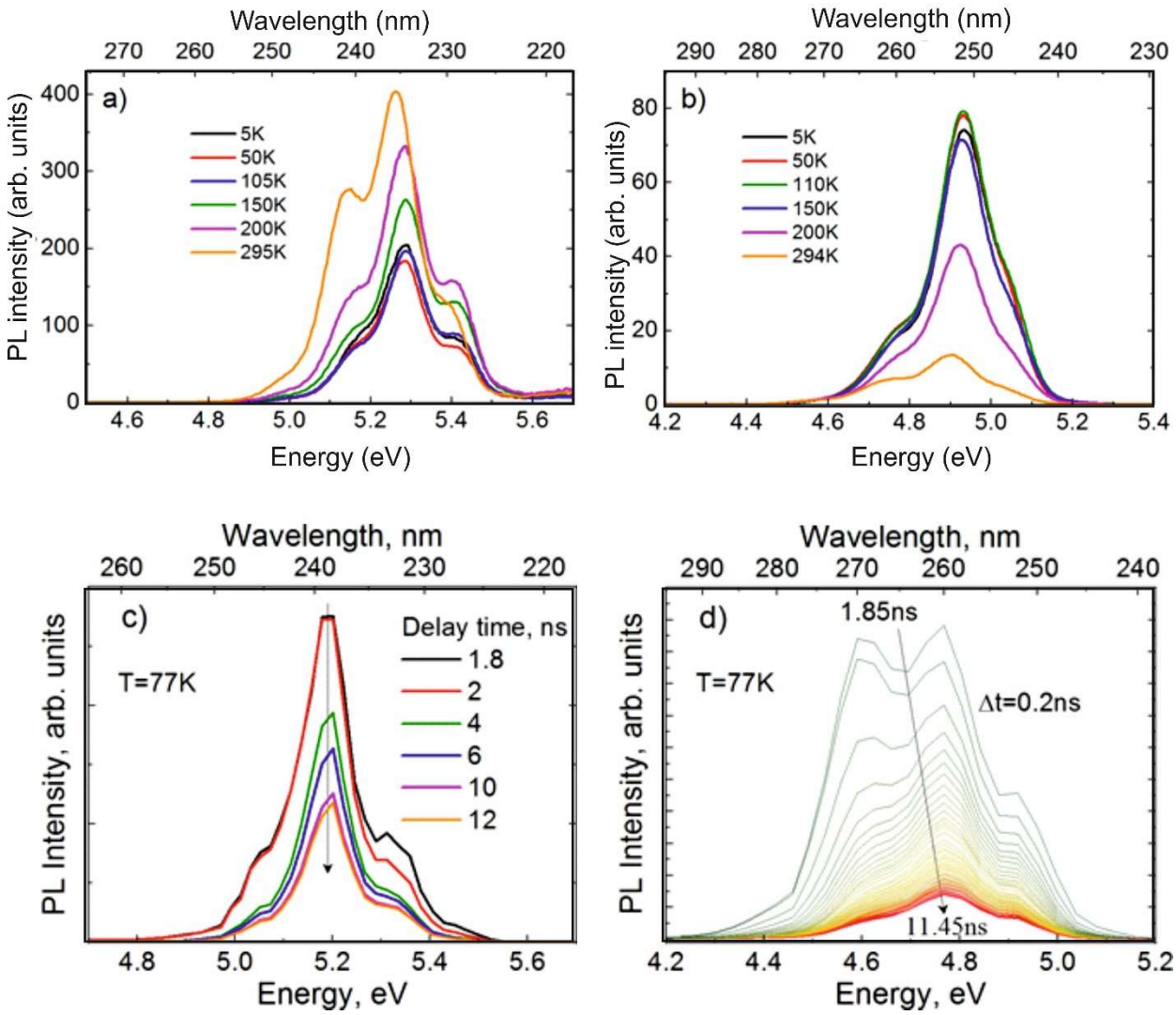

Figure S1. (a,b) Time-integrated PL spectra measured at different temperatures in GaN/AlN structures with the GaN effective thicknesses of (a) 1-2 MLs and (b) 2-3 MLs. (c,d) PL spectra recorded in the 1-2 MLs (c) and 2-3 MLs (d) GaN QWs at different delay times indicated in the plots.

Selected spectra of time-integrated PL measured at different temperatures are shown in Figure S1a,b. The modulation of the spectra is induced by Fabry-Perot interference in the epitaxial buffer layers. The energy position of the main peak is consistent with the GaN QW thickness

determined by the STEM characterization. Plots (c) and (d) show the spectra measured with different delays at the temperature 77°K. Spectra in plot (d) registered through 0.2-ns intervals clearly demonstrate the unusual spectral diffusion – the shift towards higher energy instead of the conventional red shift. Such a phenomenon is possible in an array of electronically separated 2D islands of fluctuating thickness, as discussed in the main text.

3. DFT calculations of electron and hole levels

The commonly used ***k·p*** method is highly questionable for the considered QW structures which have a width of few MLs only along with the very strong difference of the material properties between GaN and AlN. Therefore, we have carried out DFT calculations. These DFT calculations were performed in all-electron WIEN2k package [19]. The convergence parameters were set to the default values, except for $G_{MAX} = 13.0$ and $R_{MT} \cdot k_{max} = 10.0$. We set the energy convergence 10^{-5} and charge convergence 10^{-4}. For the structural relaxation we use PBEsol [20] exchange-correlational functional with the k-mesh 11×11×1 and the convergence criterion for the forces 0.1 mRy/a.u. For the band structure calculations we use the mBJ Tran-Blaha exchange-correlation potential [21] including the spin-orbit interaction with the k-mesh 17×17×1. We check the numerical accuracy of the calculation by computing the lattice constants and band gaps in bulk GaN and AlN with the k-mesh 15×15×8, and with the same energy and force convergence parameters. We find that with the chosen parameters of the convergence the lattice constants agree with the experimental values within one percent error. The band gap in this scheme is underestimated for GaN about 7% and for AlN about 20%, which is reasonable for the qualitative analysis but does not allow for the quantitative comparison of DFT results with experimental data. From the calculations, we also extracted the wavefunctions to compare the states in the nanostructure with the states in bulk GaN. Note that the calculated band structures of bulk GaN and AlN are in a good agreement with other reported data, although this result was not our direct task.

The prime cell of GaN is presented in Figure S2 that is fully analogous for AlN. The Ga atoms are shown in red and N atoms are in green. The atoms and bonds outside of the prime cell are semitransparent.

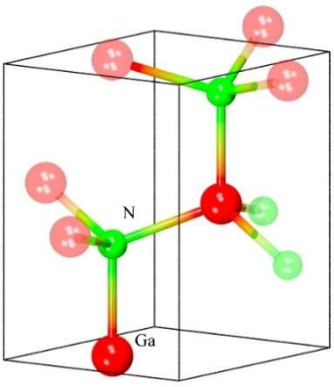

Figure S**2.** The prime cell of a wurtzite structure. Vertical direction is along the *c* axis [0001], as depicted in Ref. [22]. There are four atoms in a prime cell, below we call "monolayer" (ML) the pair of atoms C-N where C is either Ga or Al shown by large red spheres. One full period of the wurtzite crystal along the c-axis consists of 2 MLs.

In Figure S3, we show the electron density for the states (a) at the top of the valence band (for the sake of simplicity we neglect the spin-orbit interaction in the plot, while it has been included in the band structure calculations) and (b) at the bottom of the conduction band in Γ point. At atomic level, the shape of the wavefunction shows pronounced localization near a nitrogen atom, which is $p_{x,y}$-like for states in the valence band and s-like for states in the conduction band.

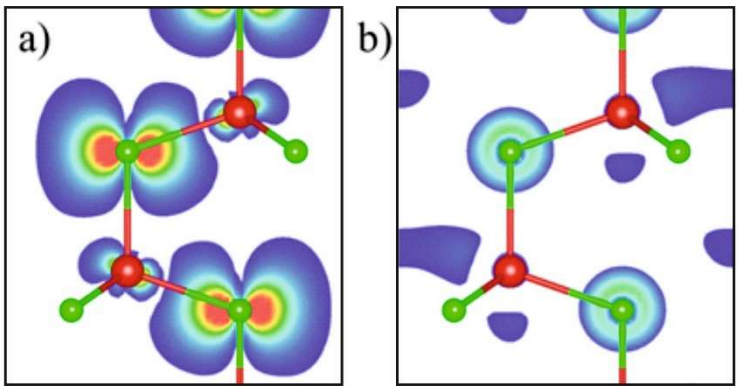

Figure S**3.** Amplitude of the wavefunction in the bulk GaN in Γ point in the [1120] plane: This plane goes through all atoms inside the prime cell shown in Figure S2. Panel (a) shows the state at the top of the valence band and panel (b) represents the state at the bottom of the conduction band. The color notations of atoms are the same as in Figure S2.

In calculations we use a 9 ML supercell, which is enough to avoid any boundary effects. The electron and hole densities for the Kohn-Sham eigenfunction for the structure with one atomic

layer (AL) of GaN inside AlN, are shown in the upper row of Figure S4. Here the color represents the electron density in the (1120) plane. The minimum values of the density are $8 \cdot 10^{-6}$ Å^{-3} for holes and $1 \cdot 10^{-6}$ Å^{-3} for electrons, these values are arbitrarily chosen for the best look. The hole wavefunction shows an ultimate degree of localization: a non-negligible amplitude can be seen only within the GaN atomic plane. The wavefunction penetration into the AlN barrier constitutes no more than a single AL. The electron wavefunction is localized weaker; it is, however, non-zero only within 2-3 MLs within the barriers. The shape of the wavefunction on the sub-atomic scale reflects the structure of electron and hole in bulk GaN in Γ point, see Figure S3. However, for the electron state, one can see a strong asymmetric shift of the wavefunction due to large electric field in the QW.

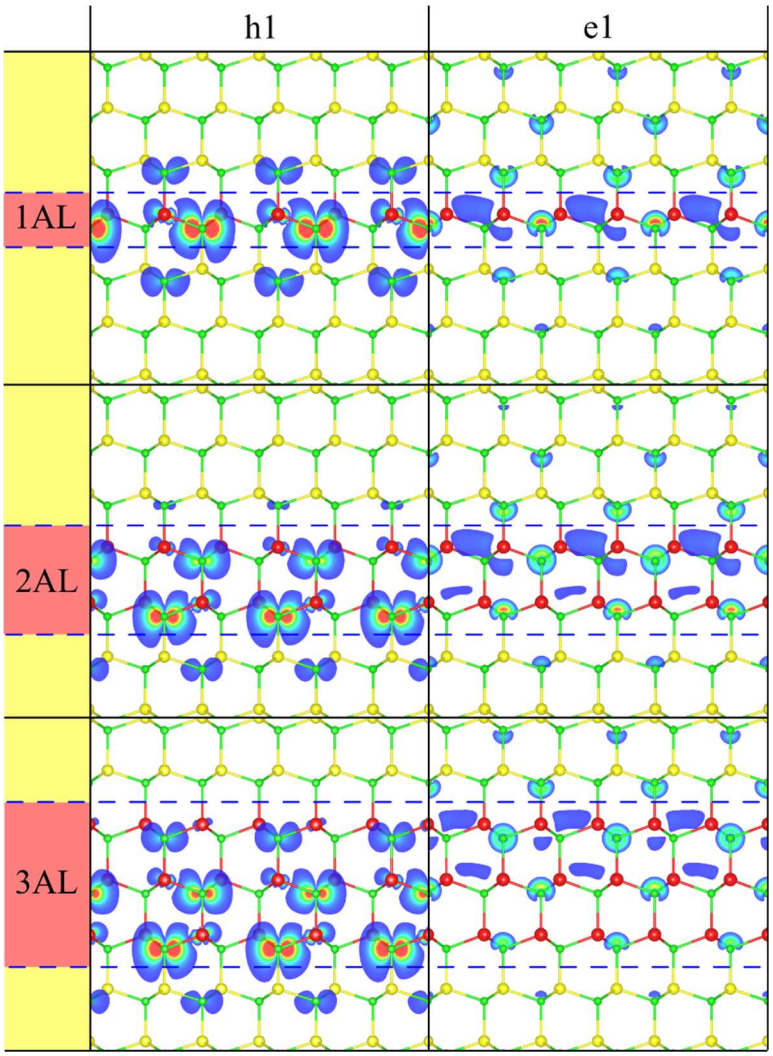

Figure S4. Amplitude of the wavefunction in the (1120) plane in the structure with 1 (upper row), 2 (middle row) and 3 (lower row) atomic layers of GaN within AlN barriers. Left panels show the ground hole level and right panels represent the ground electron level.

For the increased number of GaN MLs in the QW, the wavefunctions become somewhat less localized. In Figure S4 we show the electron density in the (1120) plane for first hole (left) and

electron (right) states in the structure with 1 (upper row), 2 (middle row) or 3 (lower row) MLs of Ga, whereas in Figure 5 of the main text we show, for the same levels and thicknesses, the electron density integrated in the lateral direction. The figures demonstrate a distinct shift of the wavefunctions towards the interfaces. The hole level is strongly localized at the "bottom" interface, and the electron wavefunction is strongly shifted towards the "upper" interface. Note that the DFT results are surprisingly similar to a qualitative analysis which can be done within the ***k·p*** theory.

4 Symmetry analysis and calculation of exciton fine structure

To describe the integral and time-resolved exciton PL we should first elucidate the exciton fine structure in the ultra-thin GaN/AlN QWs. Bulk wurtzite GaN is described by the C_{6v}^4 space group, and extrema of both conduction and valence bands are in the Γ point of the Brillouin zone [23]. The conduction band has Γ_7 symmetry. The valence band is split into three subbands: A, B, and C, which have the symmetries Γ_9, Γ_7, and Γ_7, respectively (Figure S5a). The states of the valence band at Γ point are formed mainly from *p*-type orbitals, which we denote as *X, Y* and *Z* [24]. The states of the conduction band are formed by *s*-type orbitals (S).

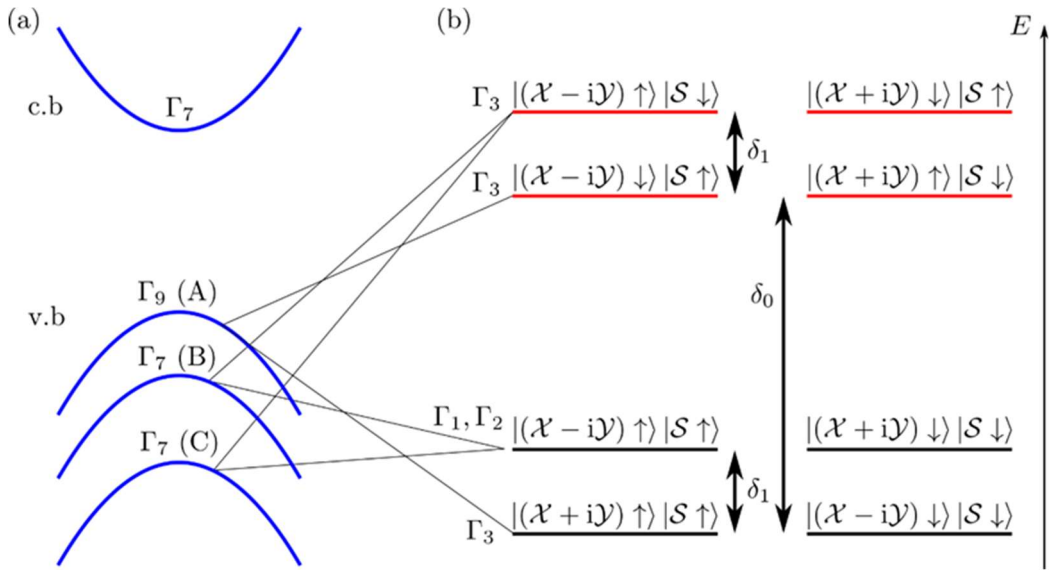

Figure S5. (a) Schematic band structure of wurtzite GaN and representations of the states in the C_{6v} point symmetry group. (b) Fine structure of e_1h_1 excitonic states in the atomically thin GaN QW and representations of the states in the C_{3v} point group. Hole and electron states are indicated in the first and second kets, respectively. Thin lines indicate origin of the hole states involved in the excitons.

A GaN/AlN QW is described by the point symmetry group C_{3v}. The representations of the lowest excitonic states e_1h_1 can be found using the compatibility and multiplication tables for the C_{3v} group [25]. The strong size quantization pushes up Z orbitals towards higher energies by a few hundreds of meV. The corresponding four excitonic states have the symmetries Γ_1, Γ_2, and

Γ_3. We will disregard these states in the following. The eight ground excitonic states are shown in Figure S5b. Three pairs of these states have Γ_3 symmetry and the two states have the symmetries Γ_1 and Γ_2. The splitting between the latter states appears due to the spin-orbit mixing with the remote bands, so we neglect it.

The dominant contribution to the exciton fine structure in narrow QWs is given by the short-range electron-hole exchange interaction [4]. In the effective mass approximation, the Hamiltonian of the short-range exchange interaction can be written as

$$H_{short} = -\varepsilon_0 \Omega_0 \delta(\boldsymbol{r}_e - \boldsymbol{r}_h) \sigma_z^e \sigma_z^h \,, \tag{3}$$

where Ω_0 is the elementary cell volume, $\sigma_z^{e,h}$ are the Pauli matrices acting on the electron and hole pseudospin, ε_0 is the short-range exchange interaction constant, which is positive in most semiconductors, and $\delta(\mathbf{r}_e - \mathbf{r}_h)$ represents the Dirac delta-function of the difference of electron and hole coordinates. The short-range exchange interaction splits the states into two groups: in the lowest excitonic states the spins of an electron and a hole are parallel, and in the upper states the spins are antiparallel, see Figure S5b. The lowest states in each group originate from the valence subband A and the upper states originate from the mixed B and C subbands; the corresponding splitting $\delta_1 = 2\Delta_2$ can be calculated using the $\boldsymbol{k}\cdot\boldsymbol{p}$ model [24]. In fact, it is of the order of the A-B exciton splitting and approximately amounts to 7.8 meV. The states with the symmetry Γ_3 can be optically active in the polarizations σ^+ and σ^-, and the state with the symmetry Γ_1 can be active in z polarization.

In Figure S5b, the first ket vector describes the hole orbital function and spin (here we use the mixed electron-hole representation), and the second ket describes the electronic spin. The dipole-allowed transitions conserve the total spin in the system, so the spins of the optically excited electron and hole should be opposite. The corresponding states belong to the group with the higher energy and are shown in Figure S5b by the red lines. The states in the other group can be active only because of the mixing with the remote bands. For example, the states with the symmetry $\Gamma_{1,2}$ can mix with the states originating from Z orbitals by the hole spin-orbit interaction. The states with the symmetry Γ_3 can weakly mix with the bright states.

The exciton binding energy is calculated to exceed the longitudinal optical phonon energy $E_{LO} \approx 100$ meV a few times [16, 26]. Therefore, we use the high frequency dielectric constant $\epsilon_\infty \sim 5$ (average for the AlGaN system) to estimate the 2D exciton Bohr radius. This gives $a_{2D} = \frac{\hbar^2 \epsilon_\infty}{2\mu e^2} \approx 4.4$ Å, where we used the reduced mass $\mu = 0.3 m_0$ [16]. Although the a_{2D} value is of the order of the lattice constant $a_0 = 2.9$ Å, we still use the effective mass approximation:

$$\delta_0 = \frac{4a_0^2}{\pi a_{2D}^2} I \varepsilon_0, \tag{4}$$

where I is the probability to find electron and hole in the same ML. In order to estimate it we divide the supercell into the elementary cells along z direction and obtain

$$I = \sum_n P_n^e P_n^h, \tag{5}$$

where n enumerates the elementary cells and

$$P_n^{e,h} = \int_{\Omega_n} \left|\psi_{e,h}(\boldsymbol{r})\right|^2 d\boldsymbol{r} \tag{6}$$

are the probabilities to find electron or hole in the cell n, which can be simply calculated as the integrals over the corresponding elementary cell Ω_n of the squared free electron and hole wavefunctions $\psi_{e,h}(\boldsymbol{r})$, respectively. The DFT calculation yields $I = 0.37,\ 0.27,$ and 0.18 for 1, 2 and 3 MLs of GaN, respectively. We determine the parameter ε_0 from the comparison of these values and the respective splitting derived from the experiment. Note, that results of DFT calculations on the energies of optical transitions are significantly underestimated. We attribute this difference to the fact that even though the mBJ scheme is in a good agreement with the band gap of basic semiconductors including GaN and AlN [27], there is a significant error in the determination of electron and hole masses [28]. In our case, this error leads to a significant error in the quantum confinement energy and, as a result, the obtained transition energies are underestimated. To compensate for this error, we shift the transition energies by 650 meV. Then, using $\varepsilon_0 = 160$ meV we perfectly fit the experimental data on the dark-bright exciton splitting. The results are presented in Figure 4c in the main text.

To check the validity of our approach, we calculate and compare with the literature data the splitting between Γ_5 and Γ_6 A exciton states in bulk GaN, using the anisotropic model for 3D excitons [29]:

$$\delta_0^{3D} = \frac{2\Omega_0^2}{\pi a_B^3 \sqrt{\eta}}\, \varepsilon_0, \tag{7}$$

where Ω_0 is the elementary cell volume, a_B is the 3D exciton Bohr radius, and $\eta = \sqrt{\varepsilon_\infty^\perp / \varepsilon_\infty^\parallel}$ with $\varepsilon_\infty^\perp, \varepsilon_\infty^\parallel$ being the high frequency dielectric constants in the directions perpendicular and parallel to the c axis, respectively. In this model, the Bohr radius is given by

$$a_B = a_B^0 \frac{\varepsilon_\infty}{\mu}, \tag{8}$$

where a_B^0 is the hydrogen atom Bohr radius, $\varepsilon_\infty = \sqrt{\varepsilon_\infty^\perp \varepsilon_\infty^\parallel}$, and

$$\frac{1}{\mu} = \frac{2+\eta}{3m_e} + \frac{1}{3}\left(\frac{2}{m_h^\perp} + \frac{\eta}{m_h^\parallel}\right), \tag{9}$$

where m_e is the electron effective mass, and $m_h^{\parallel,\perp}$ are the hole effective masses in the directions parallel and perpendicular to the c axis, respectively. For parameters taken from [29], we obtain $a_B = 32.6$ Å. Using $\Omega_0 = 21$ Å^3 and the found value $\varepsilon_0 = 160$ meV we derive $\delta_0^{3D} = 60$ μeV,

which is only two times smaller than that in Refs. [29,30]. For the values reported in Refs. [31,32,33], the order-of-magnitude matching is reasonable. In view of the crudeness of these estimations, we find such an agreement satisfactory.

5 Exciton recombination dynamics

We calculate an effective radiative lifetime $\langle\tau_{eff}\rangle$ by statistically averaging the radiative decay rates over all involved lowest-energy dark and bright excitons as

$$\langle\tau_{eff}\rangle^{-1} = \frac{\sum_i \langle\tau_i\rangle^{-1} e^{-E_i(0)/k_B T}}{\sum_i e^{-E_i(0)/k_B T}}, \tag{10}$$

where the average radiative lifetimes of excitons $\langle\tau_i\rangle$ in a state i at temperature T are the fitting parameters. For bright excitons, $\langle\tau_i\rangle$ can be related to the intrinsic radiative exciton lifetime τ_{rad}^0, the optical window width E_0, and temperature T by Eq. (1). For the spin-forbidden dark excitons, $\langle\tau_i\rangle$ is much longer. To simplify the fitting procedure, we set decay times $\langle\tau_i\rangle$ equal within the two groups of both bright (τ_b) and dark (τ_d) excitons. The fitting results only weakly depend on the value of δ_1 (see Figure S5) and we fix it as 7.8 meV. An important parameter is the energy gap separating lowest dark and bright exciton levels (δ_0 in Figure S5), which is a function of the QW width. In addition to the radiative decay, the kinetics of photoexcited carriers can be affected by nonradiative recombination. In semiconductor nanostructures based on GaN, the nonradiative decay is usually ascribed to the thermally-activated transport of carriers towards nonradiative recombination centers, such as threading dislocations and point deffects. Therefore, we simulate the nonradiative decay rate $\Gamma_{nr} = 1/\tau_{nr}$ by statistical averaging in a two-level model [34] with the fitting parameters δ_{nr}, $\Gamma_{nr,0}$ defining the respective activation energy and saturated rate of the nonradiative recombination.

The relevant experimental data used for the fitting of the emission kinetics are represented by the temperature dependence of the decay time constant τ_s, corresponding to the slowest stage of the PL decay, extracted within a biexponential decay model from the respective decay curves (like those represented in Figure 3c,d in the main text). The experimental values are fitted as

$$\frac{1}{\tau_s(T)} = \frac{1}{\tau_{eff}(T)} + \frac{1}{\tau_{nr}(T)}. \tag{11}$$

The obtained fits for a set of PL decay curves for different effective QW widths are presented in Figure 4b of the main text. All fitting parameters have clear physical meanings and can be reliably extracted from the experimental data. For example, the saturation value of τ_s at the lowest temperatures $\tau_s(0)$ gives the value of the average intrinsic lifetime of the (only populated) ground dark exciton level (τ_d). As shown in Figure 4b of the main text, the value of $\tau_s(0)$ in the thinnest insertion is rather long (~54 ns at the wavelength 230 nm), but still finite that could be partly

explained by weak residual inter-site hopping of localized excitons, accompanied by their dark-to-bright conversion. Besides, the optical transitions involving dark excitons can become weakly allowed due to the states mixing, as discussed in Section 4, or some assisted processes, such as phonon and impurity scattering.

However, inter-site hopping or phonon- and impurity-assisted processes can hardly explain the observed strong decrease of $\tau_s(0)$ with increasing the emission wavelength, i.e. for wider insertions. The increase of the GaN width from 1-2 MLs to 3-4 MLs results in the reduction of $\tau_s(0)$ by more than twice from 54 ns to 20 ns. Possible reason for reducing the emission lifetime in wider insertions can be the strongly enhanced polarization of the electron and hole wavefunctions (the quantum-confined Stark effect [35,36]), that is expected to decrease the exciton binding energy and make them subject to screening by LO phonons and free carriers [16]. Under these conditions, exciton dissociation becomes more efficient and the balance between the exciton and free-carrier populations is shifted towards the latter one, partly lifting the exciton selection rules. From Figure 4 (a) in the main text we can roughly estimate the emission wavelength separating these two regimes as ~240 nm. This energy is related to the emission of a ~2 ML thick GaN/AlN QW.

The measured saturation value of τ_s at the highest temperatures reflects the average relaxation rate, including both radiative and nonradiative contributions. The fitting results show that in the sample with the thinnest insertion the temperature-activated nonradiative recombination is negligibly weak and the excitonic radiative channels are dominant up to 300 K, whereas in the thickest QWs the nonradiative recombination is essential in the whole range of temperatures. Finally, the shape of the dependence in the range of intermediate temperatures reflects value of the characteristic activation energy δ_0. The parameter δ_0 extracted from the fit of experimental data for different samples as a function of the emission wavelength is shown in Figure 4c of the main text. All the points in the plot perfectly comply with a monotonic dependence, thus demonstrating a continuous increase of δ_0 from ~10 meV for the ~4 ML thick insertions up to ~42 meV for the thinnest (~1 ML thick) insertion. Within the spectral contour of the emission line measured at each sample, δ_0 monotonically increases with decreasing wavelength, confirming the assumption of uncoupled areas of exciton localization with a progressively increasing strength of the quantum confinement in the sites associated with excitons measured in the high energy range. One should, nevertheless, emphasize that Eq. (10) used in the fitting procedure implies implementation of a particular excitonic system and ignores contributions from the free-carrier recombination, which does not follow the selection rules specific for excitonic states. Therefore, quantitative evaluation of the involved parameters can be related only to the data obtained in the thinnest (1-2 MLs thick)

GaN/AlN insertions, where the excitonic contribution to the emission decay appears to be dominating.

The room-temperature radiative lifetime of ~5 ns, registered in the sample with a 1-2 ML thick insertion is among the shortest values detected in semiconductor QW structures. It is, nevertheless, much longer than the value 130 ps estimated for the radiative window $E_0 = 290$ μeV and $\tau_{rad}^0 = 0.6$ ps, evaluated for the parameters of bulk GaN (see Section 1). This calculated value is, however, based on several parameters with very large uncertainties including use of bulk GaN effective masses, which can be essentially different in the ultra-narrow GaN/AlN QW, and very rough estimation of the exciton lifetime at small wave-vectors. Besides, $k_B T$ energy at room temperature is still smaller than the estimated activation energy of ~40 meV and both radiative lifetime and emission intensity at 300 K are not completely saturated, as clearly seen in Figure 4a of the main text.

To perform simulation of the PL integral intensity versus temperature, we consider the experimental data on the emission intensity (Figure 4a of the main text) and the slow PL decay time (Figure 4b of the main text) simultaneously. We assume that the emission process is equilibrium and the PL integral intensity is directly proportional to the internal emission yield. At the lowest temperatures (below ~100 K), the emission yield is governed by the residual radiative decay $\tau_{d,r}$, which is relevant to dark excitons alone, since the bright excitonic states are not populated. The enhanced temperature results in an increase in the emission yield that is possible only if Γ_{nr} is nonzero. Then, the PL decay constant τ_d reads as

$$\frac{1}{\tau_d} = \frac{1}{\tau_{d,r}} + \frac{1}{\tau_{d,nr}}, \tag{12}$$

where both $\tau_{d,r}$ and $\tau_{d,nr}$ should be longer than τ_d. One of these quantities should be considered as an independent fitting parameter. One more fitting parameter is the proportionality coefficient between the measured time- and spectrally-integrated PL intensity and the internal emission yield. This quantity reflects the output efficiency of the emission and generally is unknown.

The parameters τ_b and τ_d do not depend much on the emission energy within the inhomogeneously broadened emission line and are independently estimated from fitting the respective emission decay kinetics at the line maximum. The parameters δ_0, δ_{nr}, on the other hand, depend on the emission wavelength and their average values, involved in the fitting procedure, are considered as independent fitting parameters. Such modeling of the experimentally measured integrated PL intensity versus temperature allows simulation of the emission internal quantum yield in an absolute scale (see the scale of the right axis in Figure 4a of the main text), giving for the thinnest insertion at 300°K the value as large as 75%. The corresponding decay parameters are $\tau_d = 45$ ns, $\tau_{d,r} = 140$ ns, and $\tau_{d,nr} = 66$ ns. Thus, some nonradiative decay channel is

dominating in the QW emission at the lowest temperatures, whereas thermal activation of the bright excitonic states gives rise to the enhanced both radiative decay and internal emission yield.

The curves in Figure 4a of the main text are simulated using best fits of the independent set of parameters (δ_0, $\delta_{nr}, \tau_b, \tau_d, \Gamma_{nr,0}$), describing both radiative and nonradiative recombination rates. Remarkably, the simple model implying thermally activated radiative and nonradiative recombination channels consistently describes both the temperature-induced increase of the emission integral intensity in the thinnest QWs and the emission quenching in the thickest ones. The shape of the experimental dependences can be perfectly reproduced, whereas quantitative conclusions are somewhat doubtful because the validity of the pure exciton model in the thick insertions is under question.

References

[1] Feldmann, J.; Peter, G.; Gőbel, E. O.; Dawson, P.; Moore, K.; Foxon, C.; Elliott, R. J. Linewidth dependence of radiative exciton lifetimes in quantum wells. *Phys. Rev. Lett*. **1987**, 59, 2337.

[2] Andreani, L. C.; Tassone, F.; Bassani, F. Radiative lifetime of free excitons in quantum wells. *Solid State Commun*. **1991**, 77, 641.

[3] Andreani, L. C. *Optical Transitions, Excitons, and Polaritons in Bulk and Low-Dimensional Semiconductor Structures. In Confined Electrons and Photons*, NATO ASI Series (Series B: Physics), vol. 340; Burstein, E.; Weisbuch, C., Eds.; Springer: Boston MA, **1995**.

[4] Ivchenko, E. L. Optical spectroscopy of semiconductor nanostructures; Alpha Science: Harrow UK, **2005**.

[5] Bastard, G.; Mendez, E. E.; Chang, L. L.; and Esaki, L. Exciton binding energy in quantum wells. *Phys. Rev. B* **1982**, 26, 1974.

[6] Deveaud, B.; Clérot, F.; Roy, N.; Satzke, K., Sermage, B.; Katzer, D. S. Enhanced Radiative Recombination of Free Excitons in GaAs Quantum Wells. *Phys. Rev. Lett.* **1991**, 67, 2355.

[7] Martinez-Pastor, J.; Vinattieri, A.; Carraresi, L.; Colocci, M.; Roussignol, Ph.; Weimann, G. Temperature dependence of exciton lifetimes in GaAs/AlxGa1-xAs single quantum wells. *Phys. Rev. B* **1993**, 47, 10456.

[8] Vurgaftman I.; Meyer, J. R.; Ram-Mohan, L. R. Band parameters for III–V compound semiconductors and their alloys. *J. Appl. Phys*. **2001**, 89, 5815.

[9] Gurioli, M.; Vinattieri, A.; Colocci, M.; Deparis, C.; Massies, J.; Neu, G.; Bosacchi, A.; Franchi, S. Temperature dependence of the radiative and nonradiative recombination time in GaAs/AlxGa1-xAs quantum-well structures. *Phys. Rev. B* **1991**, 44, 3115.

[10] Mak, K. F.; Lee, C.; Hone J.; Shan, J.; Heinz, T. F. Atomically Thin MoS2: A new direct-gap semiconductor. *Phys. Rev. Lett*. **2010**, 105, 136805.

[11] Zhang, X. X.; You, Y.; Zhao, S. Y. F.; Heinz, T. F. Experimental evidence for dark excitons in monolayer WSe_2, *Phys. Rev. Lett*. **2015**, 115, 257403.

[12] Ugeda, M. M.; Bradley, A. J.; Shi, S.-F.; da Jornada, F. H.; Zhang, Y.; Qiu, D. Y.; Ruan, W.; Mo, S.-K.; Hussain, Z.; Shen, Z.-X.; Wang, F.; Louie, S. G.; Crommie, M. F. Giant bandgap renormalization and excitonic effects in a monolayer transition metal dichalcogenide semiconductor. *Nat. Mater.* **2014**, 13, 1091.

[13] Robert, C.; Lagarde, D.; Cadiz, F.; Wang, G.; Lassagne, B.; Amand, T.; Balocchi, A.; Renucci, P.; Tongay, S.; Urbaszek, B.; and Marie, X. Exciton radiative lifetime in transition metal dichalcogenide monolayers. *Phys. Rev. B* **2016**, 93, 205423.

[14] Palumm, M.; Bernardi, M.; Grossman, J.C. Exciton radiative lifetimes in two-dimensional transition metal dichalcogenides. *Nano Lett.* **2015**, 15, 2794.

[15] Rinke, P.; Winkelnkemper, M.; Qteish, A.; Bimberg, D.; Neugebauer, J.; Scheffler, M. Consistent set of band parameters for the group-III nitrides AlN, GaN, and InN. *Phys. Rev. B* **2008**, 77, 075202 (2008).

[16] Bayerl, D.; Islam, S. M.; Jones, C. M.; Protasenko, V.; Jena, D.; Kioupakis, E. Deep ultraviolet emission from ultra-thin GaN/AlN heterostructures. *Appl. Phys. Lett.* **2016**, 109, 241102.

[17] Jmerik, V. N.; Nechaev, D. V.; Toropov, A. A., Evropeitsev, E. A.; Kozlovsky, V. I.; Martovitsky, V. P.; Rouvimov, S.; Ivanov, S. V. High-efficiency electron-beam-pumped sub-240-nm ultraviolet emitters based on ultra-thin GaN/AlN multiple quantum wells grown by plasma-assisted molecular-beam epitaxy on c-Al2O3. *Appl. Phys. Express* **2018**, 11, 091003.

[18] Ivanov, S. V.; Nechaev, D. V.; Sitnikova, A. A.; Ratnikov, V. V.; Yagovkina, M. A.; Rzheutskii, N. V.; Lutsenko, E. V.; Jmerik, V. N. Plasma-assisted molecular beam epitaxy of Al(Ga)N layers and quantum well structures for optically pumped mid-UV lasers on c-Al_2O_3. *Semicond. Sci. Technol*. **2014**, 29, 084008.

[19] Blaha, P.; Schwarz, K.; Madsen, G. K. H.; Kvasnicka, D.; Luitz, J. *WIEN2K, An augmented plane wave local orbitals program for calculating crystal properties*. Karlheinz Schwarz, Techn. Universit. Wien, ISBN 3-9501031-1-2 Austria, **2001**.

[20] Perdew, John P.; Ruzsinszky, Adrienn; Csonka, Gábor I.; Vydrov, Oleg A.; Scuseria, Gustavo E.; Constantin, Lucian A.; Zhou, Xiaolan; Burke, Kieron Restoring, Restoring the Density-Gradient Expansion for Exchange in Solids and Surfaces, Phys. Rev. Lett. **2008**, 100, 136406.

[21] Tran, F.; Blaha, P. Accurate Band Gaps of Semiconductors and Insulators with a Semilocal Exchange-Correlation Potential. *Phys. Rev. Lett.* **2009**, 102, 2264.

[22] Zúñiga-Pérez, J.; Consonni, V.; Lymperakis, L.; Kong, X.; Trampert, A.; Fernández-Garrido, S.; Brandt, O.; Renevier, H.; Keller, S.; Hestroffer, K.; Wagner, M. R.; Reparaz, J. S.; Akyol, F.; Rajan, S.; Rennesson, S.; Palacios, T.; Feuillet, G. Polarity in GaN and ZnO: Theory, measurement, growth, and devices, *Appl. Phys. Rev.* **2016**, 3, 041303.

[23] Bir, G. I.; Pikus, G. E. *Symmetry and Strain-Induced Effects in Semiconductors*; Wiley: New York, **1974**.

[24] Punya, A.; Lambrecht, W. R. L. Valence band effective-mass Hamiltonians for the group-III nitrides from quasiparticle self-consistent GW band structures. *Phys. Rev. B* **2012**, 85, 195147.

[25] Koster, G. F., Wheeler, R. G., Dimmock, J. O., and Statz, H. Properties of the thirty-two point groups; MIT Press: Cambridge, **1963**.

[26] Adachi, S. Properties of semiconductor alloys: group-IV, III-V and II-VI semiconductors; Wiley: Chichester, **2009**.

[27] Tran, F.; Blaha, P. Accurate band gaps of semiconductors and insulators with a semilocal exchange-correlation potential. *Phys. Rev. Lett.* **2009**, 102, 2264.

[28] Kim, Y.-S.; Marsman, M.; Kresse, G.; Tran, F.; Blaha, P. Towards efficient band structure and effective mass calculations for III-V direct band-gap semiconductors, *Phys. Rev. B* **2010**, 82, 205212.

[29] Rodina, A. V.; Dietrich, M.; Göldner, A.; Eckey, L.; Hoffmann, A.; Efros, A. L.; Rosen, M.; Meyer, B. K. Free excitons in wurtzite GaN. *Phys. Rev. B* **2001**, 64, 115204.

[30] Hoffmann, A.; Eckey, L. Excitonic fine structure and high density effects in GaN. *Materials Science Forum* **1998**, 264, 1259.

[31] Julier, M.; Campo, J.; Gil, B.; Lascaray, J. P.; and Nakamura, S. Determination of the spin-exchange interaction constant in wurtzite GaN. *Phys. Rev. B* **1998**, 57, R6791.

[32] Paskov, P. P.; Paskova, T.; Holtz, P. O.; and Monemar, B. Spin-exchange splitting of excitons in GaN. *Phys. Rev. B* **2001**, 64, 115201.

[33] Stępniewski, R.; Potemski, M.; Wysmołek, A.; Pakuła, K.; Baranowski, J. M.; Łusakowski, J.; Grzegory, I.; Porowski, S.; Martinez, G.; Wyder, P. Symmetry of excitons in GaN. *Phys. Rev. B* **1999**, 60, 4438.

[34] Neogi, A.; Morkoç, H.; Kuroda, T.; Tackeuchi, A.; Kawazoe, T.; Ohtsu, M. Exciton localization in vertically and laterally coupled GaN/AlN quantum dots. *Nano Lett.* **2005**, 5, 213.

[35] Wood, C.; Jena, D. *Polarization effects in semiconductors from ab initio theory to device applications*; Springer: New York, 2008.

[36] Im, J. S.; Kollmer, H.; Off, J.; Sohmer, A.; Scholz, F.; Hangleiter, A. Reduction of oscillator strength due to piezoelectric fields in GaN/AlxGa1−xN quantum wells, *Phys. Rev. B* **1998**, 57, R9435.